

# The Göttingen Solar Radial Velocity Project

## Sub- $\text{m s}^{-1}$ Doppler precision from FTS observations of the Sun as a star

U. Lemke<sup>1,\*</sup> and A. Reiners<sup>1</sup>

Institut für Astrophysik, Friedrich-Hund-Platz 1, 37077 Göttingen, Germany

Received; accepted

### ABSTRACT

Radial velocity observations of stars are entering the sub- $\text{m s}^{-1}$  domain revealing fundamental barriers for Doppler precision experiments. Observations of the Sun as a star can easily overcome the  $\text{m s}^{-1}$  photon limit but face other obstacles. We introduce the Göttingen Solar Radial Velocity Project with the goal to obtain high precision ( $\text{cm s}^{-1}$ ) radial velocity measurements of the Sun as a star with a Fourier Transform Spectrograph. In this first paper, we present the project and first results. The photon limit of our 2 min observations is at the  $2 \text{ cm s}^{-1}$  level but currently limited by strong instrumental systematics. A drift of a few  $\text{m s}^{-1} \text{ h}^{-1}$  is visible in all observing days probably caused by vignetting of the solar disk in our fibre coupled setup, and imperfections of our guiding system adds further offsets in our data. Binning the data into 30 min groups shows  $\text{m s}^{-1}$  stability after correcting for a daily and linear instrumental trend. Our results show the potential of Sun-as-a-star radial velocity measurements that can possibly be achieved after a substantial upgrade of our spectrograph coupling strategy. Sun-as-a-star observations can provide crucial empirical information about the radial velocity signal of convective motion and stellar activity, and on the wavelength dependence of radial velocity signals caused by stellar line profile variations.

**Key words.** instrumentation: spectrographs — methods: observational — techniques: radial velocities — spectroscopic — Sun: photosphere

### 1. Introduction

High precision radial velocity observations of the Sun as a star are important for many astronomical applications. Being the brightest object on the sky, the Sun provides enough light for very high-resolution spectroscopy that can serve as a benchmark for stellar observations. In particular, the high signal-to-noise ratio (SNR) allows high precision Doppler experiments that emulate measuring stellar radial velocities (RVs). To break the  $\text{m s}^{-1}$  barrier, solar observations are identified as important contributor for understanding the role of convection and magnetic activity in the search for extrasolar planets (e.g., Meunier et al. 2010; Dumusque et al. 2014; Marchwinski et al. 2015).

The radial velocity of the integrated Sun has been measured for many decades. Jimenez et al. (1986) used a resonance scatter spectrometer (Brookes et al. 1978) to monitor solar RVs relative to the  $\text{K I } 769.9 \text{ nm}$  absorption line achieving a precision on the order of  $\text{m s}^{-1}$ . Data from this experiment can be taken at very high cadence and is mainly used to study oscillations of the Sun but also to see variations of the solar RV over the solar cycle (Roca Cortés & Pallé 2014). High resolution spectra of the Sun as a star were obtained by Deming et al. (1987). The authors derived apparent velocities of the integrated Sun taken with the McMath Fourier Transform Spectrometer (FTS) at Kitt Peak. They found an increase in blueshift amounting to  $30 \text{ m s}^{-1}$  over three years in selected spectral lines, and they identified vignetting by the telescope optics and differential transmission as principal source of these systematic shifts. After correction, they report absolute velocities with an uncertainty of  $\lesssim 5 \text{ m s}^{-1}$ .

Wallace et al. (1988) investigated integrated light spectra from the Kitt Peak FTS taken 1976–1986. They compared spectral lines that respond differently to convective blueshift and reported upper limits of  $5 \text{ m s}^{-1}$  for secular variations of blueshift. A few years later, Deming & Plymate (1994) showed additional results from their integrated sunlight measurements reporting temporal dependence of the solar apparent radial velocity but at about half the amplitude they inferred in their earlier paper.

Another method to observe the Sun as a star is to collect its light reflected from another body, for example the Moon (e.g., Molaro et al. 2013) or moons of other planets (e.g., Molaro et al. 2015). McMillan et al. (1993) obtained solar spectra from observations of the Moon achieving Doppler precision of  $8 \text{ m s}^{-1}$  over 5 years. The advantage of this strategy is that systematic effects from vignetting are avoided. On the other hand, significantly less light can be collected so that the spectra are of lower resolution and SNR than spectra taken from direct observations of the Sun. A similar approach by Dumusque et al. (2015) uses an integrating sphere to avoid vignetting effects. They achieve a precision of  $0.5 \text{ m s}^{-1}$  for a 5 min integration time.

Sun-as-a-star observations yield high flux rates and thus enable the use of unconventional, less photon efficient techniques such as the Fourier Transform Spectroscopy. These spectrographs easily achieve spectral resolving powers at the order of  $0.5 - 1.0 \times 10^6$  while realizing a large spectral coverage spanning more than an octave. We argue that the instrument's frequency scale is steady and largely linear, thus facilitating wavelength calibration of our raw spectra (cf. Section 2.3).

At the Institut für Astrophysik Göttingen (IAG), we operate a new instrument which serves as a test-bench facility dedicated

\* ulemke@astro.physik.uni-goettingen.de

to investigate RV instrumentation and analysis methods to ultimately achieve 10 cm/s precision. We started a project to collect FTS spectra from the Sun as a star with facilities installed in our faculty building (see Reiners et al. 2015). We discuss here the potential of this new instrument concept to address the challenges of Sun-as-a star measurements while making best use of the available photon flux rates.

We aim to obtain a long-term database of spectra that can be used for a variety of applications. One of the main drivers is monitoring the solar radial velocity as initiated in the projects mentioned above. Wide wavelength coverage allows an in-depth investigation of the correlation between RV-trends and magneto-convection as a function of wavelength.

In this paper, we introduce the project reporting first results on our RV performance together with current instrument limitations.

We provide a description of our instrument and observing strategy in Section 2. We explain our data reduction and analysis scheme in Section 3 and present the first results of our RV observations in Section 4. A summary is given in Section 5.

## 2. Instrument description

On the roof of our institute building at IAG, we are operating a 50 cm siderostat that is normally used for spatially resolved solar observation. We utilize this setup to track the Sun and feed light into a fiber to transport it into our optics laboratory where the spectrum is recorded with our FTS. The instrument consists of three main parts depicted in Fig. 1: (A) the siderostat, (B) an iodine cell, and (C) the Fourier-Transform Spectrograph.

A main concern with sun as a star observations is homogeneous coupling efficiency over the extended solar disk. We therefore decided for a near field fiber-coupling strategy where the solar disk is imaged directly on the fiber core. In this configuration we can make use of the fiber's homogenization capabilities to 'scramble' the input light distribution (see Hunter & Ramsey 1992; Avila et al. 2006). This has the advantage that the risk of vignetting can be confined to a very short section of the beam, i.e. the focal plane of the focussing mirror PM1. The risk remains, however, that this setup produces spurious RV-signals if we do not succeed in coupling all points of the solar disk with equal efficiency over the entire fiber core. In fact, we encountered some systematic effects which are discussed in Section 4. The alternative of a free beam feed to the FTS on the other hand is prone to vignetting throughout a long optical path and thus more difficult to control. For a corresponding in-depth discussion the reader is referred to Deming et al. (1987); Deming & Plymate (1994).

Further design decisions include the employment of reflective mirrors for beam conversion to achieve a broad wavelength coverage of 0.5–1.0  $\mu\text{m}$ . Aperture diameters were chosen to avoid beam vignetting along the optical assembly to reduce risk of performance loss caused by fiber modal noise (Lemke et al. 2011).

### 2.1. Siderostat

The siderostat consists of two flat mirrors guiding sunlight into a 55 cm entrance window of the Vacuum Vertical Telescope (VTT<sup>1</sup>). We place the parabolic focussing mirror (PM1) after the second siderostat mirror (M2). In this configuration the pointing

**Table 1.** Technical data of the siderostat coupling. See Fig. 1 for the positions of M1, M2, and PM1.

Siderostat mirrors (flat) M1, M2	
Diameter	0.5 m
Focussing mirror, Thorlabs RC12FC-P01, PM1	
Reflective surface	Protective silver coating
Effective focal length	50.8 mm
Free aperture	22.0 mm (reduced to 13.5 mm)
Image scaling factor	490 $\mu\text{m}$ $\sim$ 32' on sky
Beam f-ratio	F/4.2
Fiber link to telescope, CeramOptec WF 880	
Diameter, core	800 $\mu\text{m}$
Fiber numerical aperture	0.22

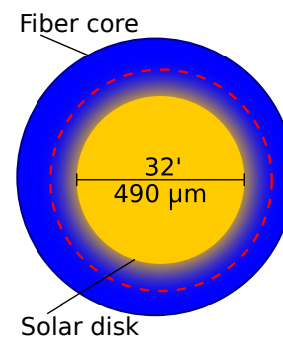


**Fig. 2.** Depiction of the relative dimensions of the solar disk image (490  $\mu\text{m}$  inner circle) and the fiber core (800  $\mu\text{m}$  outer circle) at the image plane of PM1. The dashed line signifies the area that needs to be coupled to ensure radial velocity precision (explanation see text).

of PM1 is determined by the pointing of the VVT such that we can use its automated guiding facility for solar tracking.

The two siderostat mirrors were equipped with an automated guiding mechanism in alt-azimuth mounting. During our observations, the setup performed only a coarse guiding accuracy with a drift of  $\approx$  1-3 arcmin  $\text{h}^{-1}$  requiring manual intervention. Manual tracking correction was implemented as follows: PM1 was placed in the telescope pupil and only masked a small fraction of the collimated beam, the main fraction of light was passed to the VVT. In the Coudé focus of the VVT a screen was placed for projection of the solar disk. The position of this re-imaged disk with respect to the screen was used as a measure for the pointing of the siderostat and as reference for the manual tracking correction.

PM1 creates an image of the solar disk with an average size of 490  $\mu\text{m}$  on the fiber entrance that has a diameter of 800  $\mu\text{m}$  (Fig. 2). Due to the parabolic geometry of PM1 we need to consider that non-paraxial rays originating from the edge of the solar disk will encounter strong optical aberrations. We simulated the optical performance and found that a larger circular area of 40' width (620  $\mu\text{m}$ ) needs to be coupled to ensure 30  $\text{cm s}^{-1}$  RV-precision, leaving a margin for manual guiding of approx. 6' in each direction. We estimated our tracking accuracy to be better than 2' and therefore did not expect significant RV-errors from guiding inaccuracies.

If, however, homogeneous coupling over the solar disk is not achieved, systematic vignetting can occur. This produces trends in the RV-signal which correlates to the manual tracking correction. Moreover, the RV-signal becomes a function of the hour-

<sup>1</sup> <https://www.uni-goettingen.de/en/217813.html>

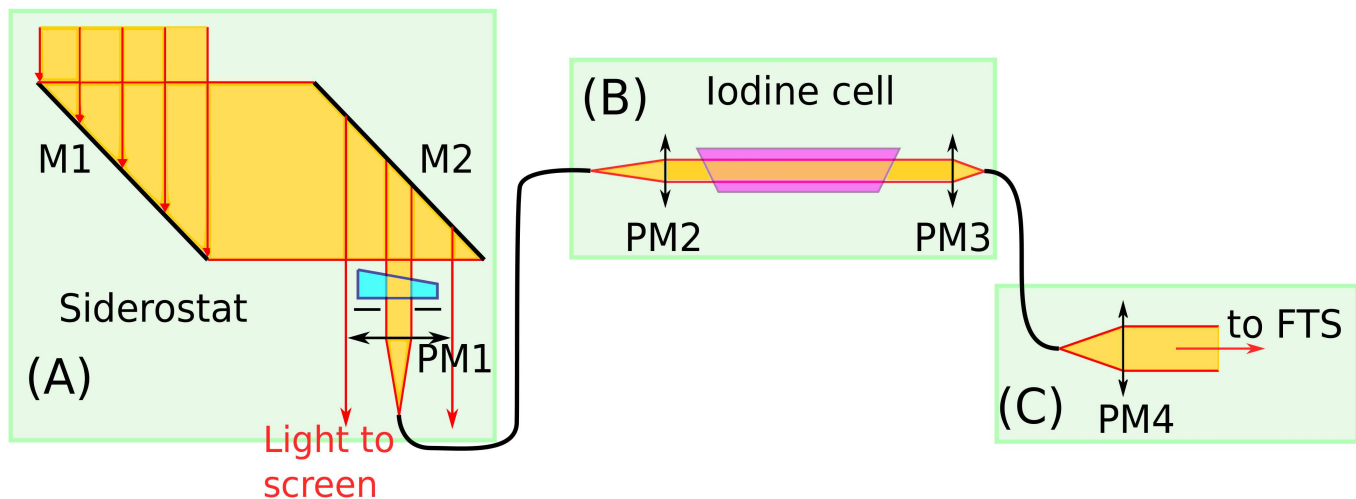


**Fig. 1.** Overview of the instrument: (A) Siderostat unit, consisting of plane mirrors M1, M2 and parabolic mirror PM1 to focus light onto a fiber which links the telescope to an iodine cell; (B) a set of two parabolic mirrors, PM2 and PM3 create a collimated beam and focus again to a fiber that connects the setup with the Fourier Transform Spectrograph (FTS); (C) fiber feed into the FTS.

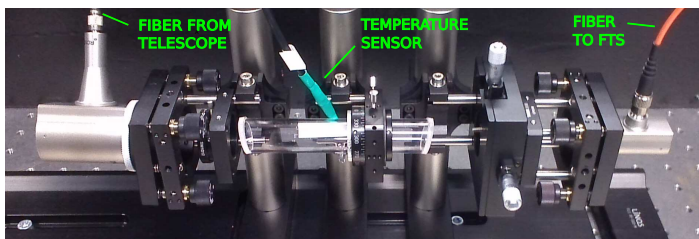


**Fig. 3.** Iodine cell setup in the optics laboratory. Light from the telescope is collimated (left), passes through the cell with two wedged and tilted windows to then be reimaged onto a second fiber that guides the light to the FTS. Temperature is recorded during measurement.

angle, because the solar disk apparent axis changes with respect to the instrument axis. Likewise, we would also expect offsets between individual dates due to the inclination of the ecliptic with respect to the solar rotation axis (cf. Section 4).

After our first experiments we realized that the amount of sunlight collected in the 22 mm free aperture substantially heats the fiber entrance. We reduced the free aperture diameter of PM1 to 13.5 mm in order to avoid damage from heating. Furthermore, a 0.5° wedged BK-7 protective window was placed in front of the parabolic mirror to prevent dust and reduce transmission of UV and infrared radiation.

## 2.2. Iodine cell

Our FTS provides internal wavelength calibration based on a stabilized HeNe laser. The accuracy of this wavelength scale is limited to several  $10 \text{ m s}^{-1}$  by the laser itself and by the optical properties of the FTS. For precision RV measurements at the  $\text{m s}^{-1}$  level, this calibration is not sufficient. In our experiment we therefore applied the absorption cell method (Butler et al. 1996) to provide a high-accuracy wavelength reference superimposed on the solar spectrum. Only the relative drift of the instrument is corrected with reference to the iodine spectrum. This creates an uncertainty in the absolute offset of the solar RV-signal at the order of few m/s. We used two parabolic mirrors (PM2

and PM3) to create a collimated beam in which we place an iodine cell; a photograph of the setup is shown in Fig. 3. The setup can accommodate other cells, e.g., for wavelength calibration in the near infrared. We operated the cell at ambient temperature of the laboratory. Variations of temperature were on the order of  $\pm 1^\circ$ , and the absorption cell provides enough RV information for  $\text{m s}^{-1}$  accuracy in our FTS spectra.

## 2.3. Fourier Transform Spectrograph

The IAG operates the IFS 125, a Fourier Transform Spectrometer (FTS) from Bruker Optics. For a discussion on Fourier transform spectroscopy the reader is referred to e.g. Griffiths & De Haseth (2007). The principle of operation is that of a two-beam Michelson interferometer with one of the mirror arms moving to introduce a controllable path difference. The intensity of the interference signal is measured by a detector as a function of path difference from which the spectrum is determined by applying the Fourier transform.

An advantage of Fourier transform spectroscopy is that it allows simultaneous coverage of a large spectral range at high spectral resolution. In particular, the instrument wavelength solution is linear across the entire wavelength range (see Reiners et al. 2015). A disadvantage with large wavelength ranges in Fourier spectroscopy is that all frequencies contribute to the photon noise. For this reason, the wavelength range is often restricted with filters. In this work we are using a very large spectral range for RV evaluation. The large number of spectral lines contributing to the RV-calculation outweighs the additional photon noise.

In order to reduce radial velocity drifts of the spectrograph, the FTS vacuum pump was under constant operation during observations to keep the pressure between 0.2 to 0.3 hPa. This further stabilizes the wavelength solution which is permanently monitored by our iodine cell.

### 3. Observations and Data analysis

#### 3.1. Observations

We observed the integrated Sun during several days between Mar and Oct 2015. For this introductory paper, we only considered three days, Apr 20, Apr 23 and Jun 05, during which the Sun could be observed for about six to eight hours each.

Other dates show similar quality in terms of RV-scatter. However, we rejected data taken under cloudy observing conditions. They can be subsequently identified by significant decrease of flux levels and are occasionally accompanied by an increase in RV-scatter because clouds passing in front of the solar disk induce a Rossiter-McLaughlin effect. It becomes significant when the characteristic time of such a cloud-passage matches our integration time of 2 min. We expect that (slowly moving) cirrus clouds have such an effect on our data.

We operated the FTS in symmetric mode with a maximum path difference of 33 cm, which realizes a nominal resolving power of  $0.03 \text{ cm}^{-1}$ , i.e.  $R = 670,000$  at  $\lambda = 5000 \text{ \AA}$  and  $R = 370,000$  at  $\lambda = 8900 \text{ \AA}$ , respectively. The duration of one scan was 1.6 min (2.0 min for Jun 05). Interferograms are Fourier transformed with the FTS standard software.

#### 3.2. Instrument wavelength solution

A preliminary frequency calibration is provided by the FTS internal HeNe reference-laser. However, the frequency scale requires some correction mainly because of the beam divergence and the deviation of optical paths between the science light beam and the reference laser. It is therefore standard in Fourier-Transform Spectroscopy to correct for this with a factor (see e.g., Griffiths & De Haseth 2007):

$$\nu = (1 + k)\nu', \quad (1)$$

with  $\nu$  being the corrected frequency and  $\nu'$  the frequency solution provided by the internal laser. In our observations we used iodine absorption lines to determine the wavenumber correction  $k$ . The correction was incorporated in our fitting procedure by utilizing the fact that  $k$  has the form of a Doppler shift,  $k \approx -v_{eff}/c$ , with  $v_{eff}$  an effective Doppler velocity and  $c$  the speed of light (see Section 3.4).

#### 3.3. Atmospheric contamination

Telluric absorption can be a problem for high-precision RV measurements (see e.g. Bean et al. 2010; Cunha et al. 2014). We paid attention to the influence of atmospheric lines and incorporated masks to minimize the effects of telluric line contamination. To achieve this, we simply exclude frequencies at which atmospheric lines show significant absorption. Using a binary mask based on the HIgh-resolution TRANsmission molecular absorption database (HITRAN<sup>2</sup>). Frequency positions with telluric line intensities  $> I_{min} = 1 \times 10^{-26} \text{ cm}^{-1}/(\text{molecule cm}^{-2})$  are masked out.

We also excluded other regions of strong telluric contamination completely from the analysis in order to ensure a stable continuum fit for our spectra:

1.  $\lambda_c = 8230 \text{ \AA}$  – a  $200 \text{ \AA}$  region, H<sub>2</sub>O contamination
2.  $\lambda_c = 7660 \text{ \AA}$  ( $130 \text{ \AA}$  width, O<sub>2</sub>)
3.  $\lambda_c = 7140 \text{ \AA}$  ( $540 \text{ \AA}$  width, H<sub>2</sub>O)

<sup>2</sup> <http://hitran.org/lbl/>

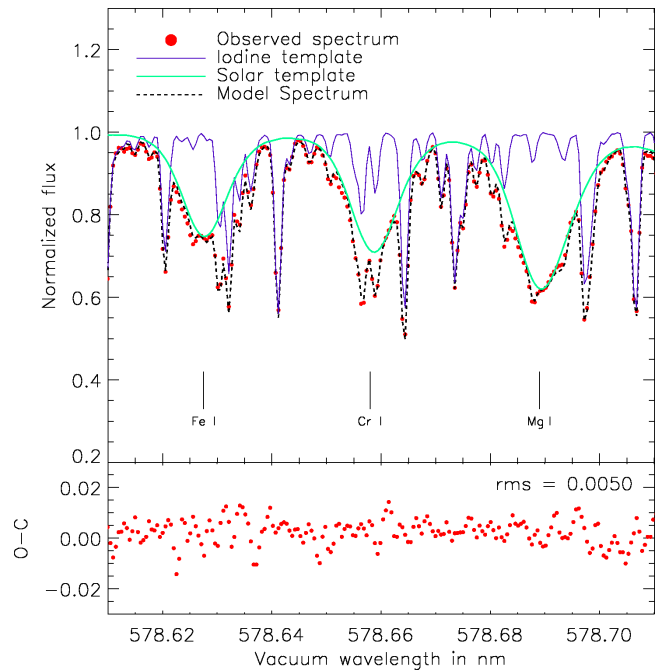


**Fig. 4.** Normalized spectra over wavelength in vacuum. The template spectra of iodine (blue) and the Sun (green) are multiplied to calculate the model (dashed) of the observation (red). Residuals between observed spectrum (O) and our model (C) are shown in the lower panel. Model and observation match within an rms of 0.5%. The locations of three solar absorption lines are indicated.

4.  $\lambda_c = 5930 \text{ \AA}$  ( $35 \text{ \AA}$  width, H<sub>2</sub>O)

We further excluded a region between  $6280 \text{ \AA}$  and  $6430 \text{ \AA}$  where features caused by the FTS reference laser as well as O<sub>2</sub> and H<sub>2</sub>O-absorption bands affect the spectrum.

#### 3.4. Doppler signal extraction

The spectrum of the Sun observed through an iodine cell can be modeled as

$$I_{\text{model}}(\nu') = p(\nu') [T_{I_2}((1 + k)\nu') \cdot I_{\odot}((1 + v_{\odot}/c)\nu')], \quad (2)$$

with  $p(\nu')$  a normalization function,  $T_{I_2}$  a spectral template containing only the iodine spectrum, and  $I_{\odot}$  an iodine free solar template spectrum. For the solar template we use observations of the Sun (iodine cell removed) collected on Mar 20 and Doppler corrected the individual spectra prior to averaging. The iodine template was recorded during the night after the solar template spectrum was taken. To do this we replaced the telescope fiber by a fiber that guides light from a tungsten lamp and co-added 100 scans with this setup. Solar and iodine template as well as the observed spectrum were normalized prior to the minimization process and therefore are not affected by the different energy distributions of both radiation sources.

In addition to a smooth polynomial that describes the continuum,  $p(\nu')$ , the only two free parameters in Eq. 2 are the Doppler correction  $k$  and the solar radial velocity  $v_{\odot}$ . To determine these parameters, we minimize  $\chi^2$  from the residual between our observed spectra and  $I_{\text{model}}$ .  $T_{I_2}$  and  $I_{\odot}$  are interpolated with a quadratic spline in order to determine the respective flux of  $I_{\text{model}}$  for the frequency grid of the observed spectrum. An example of the fit quality is shown in Fig. 4, the root-mean-square (rms) deviation between our model and an observed spectrum is 0.5% in this case.

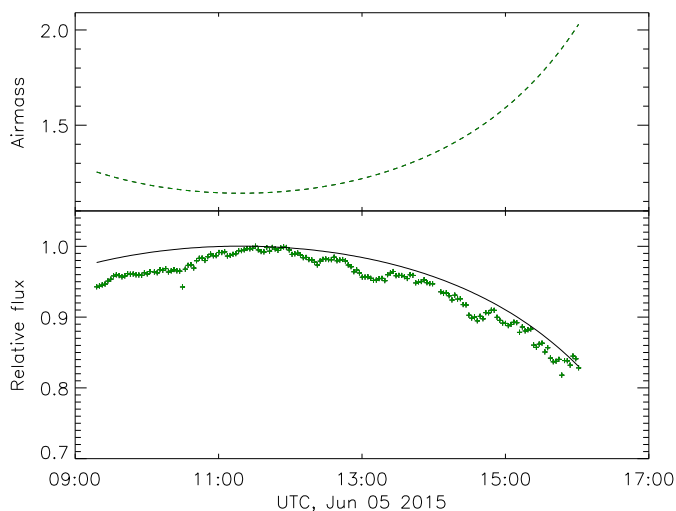


**Fig. 5.** Airmass (upper panel) and observed continuum flux at 670 nm (lower panel; green crosses) for June 05 together with the attenuation calculated from airmass assuming an extinction coefficient of 0.21.

The radial velocities presented in this paper are calculated in the wavelength range 5000 – 8900 Å. The spectrum was divided into approximately equally sized sections of  $350 \text{ cm}^{-1}$ , corresponding to  $80 \text{ Å}$  in the blue and  $200 \text{ Å}$  in the red part of the spectrum. We performed a simultaneous fit of iodine and solar spectra for  $\lambda < \lambda_{\text{HeNe}}$  (Eq. 2). For  $\lambda > \lambda_{\text{HeNe}}$  the iodine absorption is weak, therefore we performed  $\chi^2$ -minimization with  $v_{\odot}$  as a single free parameter. The  $v_{\odot}$  and  $v_{\text{eff}}$  of all regions are equally weighted to obtain the raw solar RV-signal  $v_{\text{obs}}$ .

We also tested weighing the sections according to their RV information content (Bouchy et al. 2001, cf.) which reduced the final rms at the few percent level. This points to other dominant sources of noise: We assume that e.g. towards the red part of the spectrum the iodine saturation is very temperature sensitive and therefore severely distorts the  $v_{\odot}$ -signal. Likewise, for the faint blue end of the spectrum, the iodine RV-information becomes dominant over the solar RV-information and thus is affected by the fitting uncertainty of the solar lines. While this list of effects is not exhaustive, we feel that a complex treatment of all these influences is required when ultimately aiming at sub 10 cm/s precision. At this stage of instrument development, however, the most dominant source of error is caused by imperfect coupling. We therefore concluded that the equal-weights approach is adequate for now.

### 3.5. Radial velocities in observations of integrated sunlight

Radial velocities expected for our integrated sunlight observations,  $v_{\text{obs}}$ , can be written as follows:

$$v_{\text{obs}} = v_{\text{orb}} + v_{\text{spin}} + v_{\text{grs}} + v_{\text{cb}}, \quad (3)$$

with  $v_{\text{orb}}$  the orbital velocity of Earth around the Sun,  $v_{\text{spin}}$  the velocity of the observatory caused by the rotation of Earth,  $v_{\text{grs}}$  the solar gravitational redshift, and  $v_{\text{cb}}$  the mean convective blueshift. Other components like solar pulsations can be relevant but are not considered here.

For the two components  $v_{\text{orb}}$  and  $v_{\text{spin}}$ , we started with the values provided by the NASA Horizon’s project webpage<sup>3</sup>. We

<sup>3</sup> horizons.jpl.nasa.gov

computed the weighted mean of the RV-signal for the rotating Sun by disk-integrating over the solar surface taking into account the effects of solar (differential) rotation and limb darkening.

In addition, we calculated the effects of differential transmission which occur because individual points of the extended solar disk are observed at different elevation, and thus different airmass, on sky. The resulting differential attenuation across the disk causes a net RV-signal. We determined the extinction coefficient for individual dates by fitting the observed flux at  $6700 \text{ Å}$  to the predicted trend for an observing day. An example of airmass and relative flux during observations on Jun 05, 2015 in Fig. 5. From the extinction coefficient we can determine weights for each point on the solar disk and derive the disk-integrated net RV-effect which is subsequently subtracted from our RV-results. Differential transmission becomes particularly important for observations at high airmass and results in an integrated radial velocity signal that deviates  $1 \text{ m s}^{-1}$  for observations at airmass 2 compared to zenith observations. We note that this approach is different to Deming et al. (1987), whose method of fitting a linear trend to the airmass-dependent RV can be sensitive to other systematic effects.

### 3.6. Photon noise limit

The great potential of our instrument setup is the high RV precision that can be attained. We estimate the RV precision following the calculations in Butler et al. (1996) and Bouchy et al. (2001). For the Sun, we assume the quality factor  $Q \approx 15,000$  and in our spectra we reach an SNR of 100–200 per frequency bin of  $\Delta\nu = 0.015 \text{ cm}^{-1}$  width. Using information from between 5000 and 8900 Å (excluding  $\text{H}_2\text{O}$ -bands and HeNe laser region), we estimate that the photon limit for our RV precision is approximately  $2 \text{ cm s}^{-1}$  per 1.6 min exposure.

## 4. Results

We have taken observations of integrated sunlight with an iodine cell on some 20 days between Mar and Oct 2015. In Fig. 6 we show as example three days during which continuous observations were possible under local weather conditions and without major problems during observation.

In the upper panel we show our RV measurements as derived from  $\chi^2$ -minimization (Eq. 2). We overplot the modelled barycentric velocity as calculated for the time of each observation and discussed in Section 3.5 (solid line).

In the second row of each panel in Fig. 6, we show the residuals between our RV measurements and the model. We can see a slope in all three days with a gradient of approximately  $2\text{--}5 \text{ m s}^{-1} \text{ h}^{-1}$ . In addition, there are clear systematic variations, for example a dip shortly before 14:00 on Apr 20, and sawtooth patterns with periods of a few 10 min on Apr 23 and June 05. These discontinuities occurred when the guiding had to be adjusted manually. This points to a systematic vignetting of the solar disk. A subsequent inspection of the telescope-fiber revealed slight damage at the edge of the fiber core, probably related to intense radiation and despite our efforts to reduce radiation to tolerable levels. Nevertheless, in the following we analyze the statistical quality of our daily RV measurements knowing that an improvement of our instrument setup is required to remedy the systematic problems.

The offsets in panel (b) are the relative RV-signal with respect to the barycentric corrected template and amount to  $\approx 65 \text{ m s}^{-1}$ ,  $20 \text{ m s}^{-1}$  and  $40 \text{ m s}^{-1}$  for each individual date. We in-

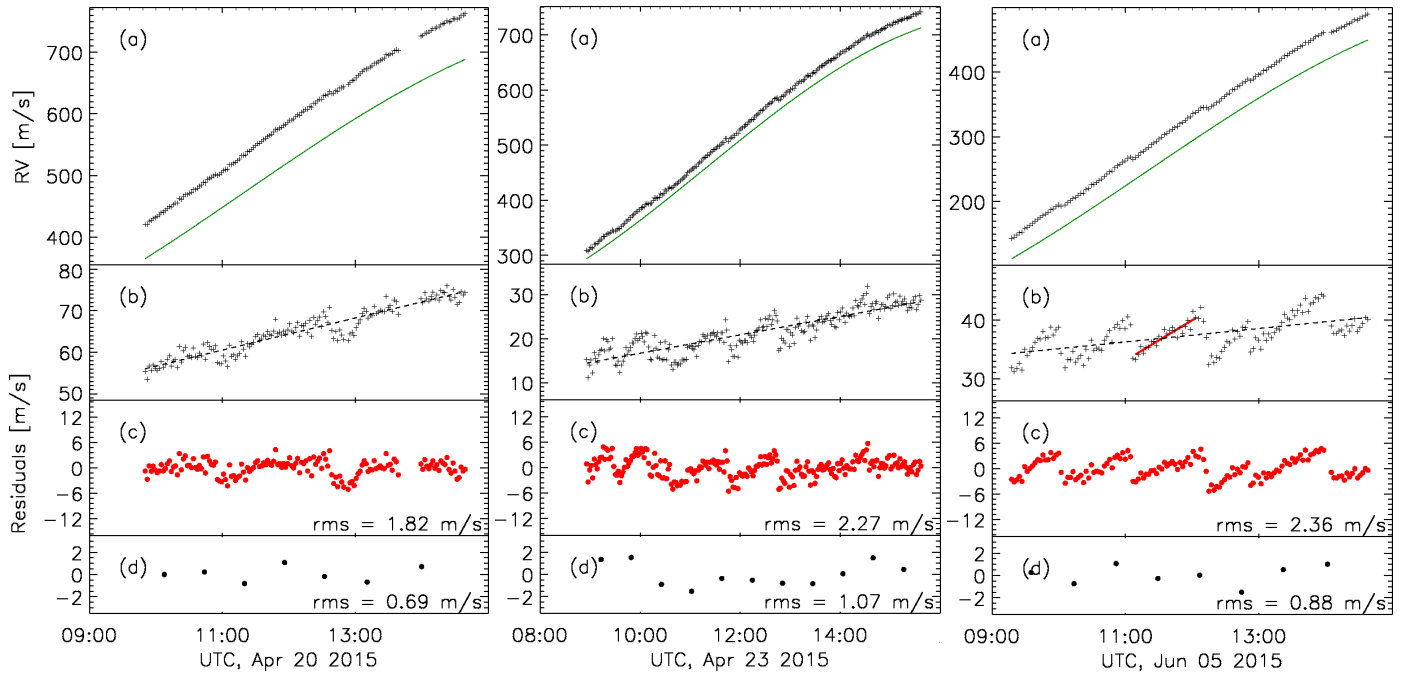


**Fig. 6.** Radial velocity signal for observations on April 20th, April 23rd and June 5th, 2015. Shown are (a) the initial RV-signal, compared to the theoretical values expected from barycentric correction and taking disk integrated effects into into account (solid line); (b) shows the residuals between observed and predicted values; (c) displays residuals after correcting for inhomogeneous coupling efficiency; The last panel (d) shows the remaining scatter after binning of individual data points ( $\sim 30$  minutes exposure time).

terprete these as being caused by the systematic vignetting (see section 2.1). While we consider this the main contribution to the observed offsets, it should be noted that the solar spectral line shape is influenced by occurrence of sunspots which creates an RV-signal of a few  $\text{m s}^{-1}$  that evolves on time scales related to the synodic period, typically at the order of several days (Dumusque et al. 2014). However, this effect is currently not observable due to the systematic vignetting effect.

We assume that systematic vignetting causes a slowly varying RV-response and remove the slope that occurs in the residuals (second row in Fig. 6) for each day by applying a linear fit. The standard deviation of the RV residuals corrected this way are reported together with the data in panel (c). Standard deviations are at the order of  $2 \text{ m s}^{-1}$  for all days but still clearly dominated by systematic effects occurring on timescales of a few 10 min, significantly longer than the sampling of our data.

We refrain from a deeper analysis of the RV scatter around the most probably systematic trends, but note how low the rms around the strong systematic effects on our high cadence data. Taking a subset of June 5 as example (solid red line in panel (c)) the rms around this linear fit is  $70 \text{ cm s}^{-1}$ .

In the bottom row of Fig. 6, we grouped the data from the third row into bins of 30 min each. This smoothes out some of the systematic effects that do not occur on regular timescales. The rms of these data indicates that observations taken during one day, and corrected for a systematic linear trend, are on the level of  $1 \text{ m s}^{-1}$ .

## 5. Summary

We have presented the first Sun-as-a-star RV-measurements using our fiber-fed Fourier Transform Spectrograph at IAG. The high spectral resolution of the instrument can potentially provide extreme RV precision of  $\approx 2 \text{ cm s}^{-1}$  at high cadence. Further-

more, the validity of the wavelength solution across the entire FTS wavelength range (including areas void of calibration lines) allows investigation of RV signals across a large spectral range.

Our first results demonstrate the potential of the FTS RV-measurements, but they also reveal a number of difficulties. Currently the limiting factor in our setup is the way the extended solar disk is coupled into the fiber. Inhomogeneous coupling of the extended solar disk causes systematic effects that are as large as several  $\text{m s}^{-1} \text{ h}^{-1}$ . After correction for these daily trends, our data reveal further jumps on the order of a few  $\text{m s}^{-1}$  but remain under  $1 \text{ m s}^{-1}$  if we group the data into bins corresponding to 30 min exposure time. We showed that the rms between individual data points is at the level of sub  $\text{m s}^{-1}$  but this high precision is not yet useful for scientific analysis because of the strong systematics.

The most dominant feature in our data is induced by the guiding and coupling of solar light. Our method involves direct imaging of the solar disk on the fiber end-face. On inspection the fiber surface revealed irregularities which are most probably linked to the vignetting effect that causes the instrument systematic behaviour. Difficulties related to inhomogeneous coupling efficiency are not new, Deming & Plymate (1994) encountered a problem of similar nature, describing it as one of the aspects of ‘The perils of integrated light’, noticing a RV drift that appears to be a function of the the hour angle that is consistent with beam-vignetting in their FTS. Their approach is different in the regard that they couple the solar light directly into the FTS whereas in this work we use a fiber optical cable.

The observation of Sun-as-a-star radial velocities at very high precision can provide crucial information on the nature of short- and long-term RV variability connected to convection, activity, and other mechanisms related to stellar phenomena, instrument components (e.g. modal noise in optical fibers) as well as analysis (e.g. masking or modelling of atmospheric lines) and

so is identified as an important step towards  $\text{cm s}^{-1}$  precision observations of stars other than the Sun. We are currently revising our coupling strategy, but already now our results show the great potential of FTS solar observations for our understanding of high-precision RV measurements.

*Acknowledgements.* We would like to thank Sandra V. Jeffers and Mathias Zechmeister for valuable scientific discussions. UL acknowledges research funding from the Deutsche Forschungsgemeinschaft (DFG) under the SFB *Astrophysical Flow Instabilities and Turbulence*, SFB 963/1, and from the Starting Grant *Wavelength Standards*, Grant Agreement Number 279347. AR acknowledges research funding from DFG grant RE 1664/9-1. The FTS was funded by the DFG and the State of Lower Saxony through the Großgeräteprogramm *Fourier Transform Spectrograph*.

## References

- Avila, G., Singh, P., & Albertsen, M. 2006, in Society of Photo-Optical Instrumentation Engineers (SPIE) Conference Series, Vol. 6269, Society of Photo-Optical Instrumentation Engineers (SPIE) Conference Series, 5
- Bean, J. L., Seifahrt, A., Hartman, H., et al. 2010, *ApJ*, 713, 410
- Bouchy, F., Pepe, F., & Queloz, D. 2001, *A&A*, 374, 733
- Brookes, J. R., Isaak, G. R., & van der Raay, H. B. 1978, *MNRAS*, 185, 1
- Butler, R. P., Marcy, G. W., Williams, E., et al. 1996, *PASP*, 108, 500
- Cunha, D., Santos, N. C., Figueira, P., et al. 2014, *A&A*, 568, A35
- Deming, D., Espenak, F., Jennings, D. E., Brault, J. W., & Wagner, J. 1987, *ApJ*, 316, 771
- Deming, D. & Plymate, C. 1994, *ApJ*, 426, 382
- Dumusque, X., Boisse, I., & Santos, N. C. 2014, *ApJ*, 796, 132
- Dumusque, X., Glenday, A., Phillips, D. F., et al. 2015, ArXiv e-prints
- Griffiths, P. R. & De Haseth, J. A. 2007, *Fourier transform infrared spectrometry*, Vol. 171 (John Wiley & Sons)
- Hunter, T. R. & Ramsey, L. W. 1992, *PASP*, 104, 1244
- Jimenez, A., Palle, P. L., Regulo, C., Roca Cortes, T., & Isaak, G. R. 1986, *Advances in Space Research*, 6, 89
- Lemke, U., Corbett, J., Allington-Smith, J., & Murray, G. 2011, *MNRAS*, 417, 689
- Marchwinski, R. C., Mahadevan, S., Robertson, P., Ramsey, L., & Harder, J. 2015, *ApJ*, 798, 63
- McMillan, R. S., Moore, T. L., Perry, M. L., & Smith, P. H. 1993, *ApJ*, 403, 801
- Meunier, N., Desort, M., & Lagrange, A.-M. 2010, *A&A*, 512, A39
- Molaro, P., Esposito, M., Monai, S., et al. 2013, *A&A*, 560, A61
- Molaro, P., Monaco, L., Barbieri, M., Zaggia, S., & Lovis, C. 2015, *The Messenger*, 161, 20
- Reiners, A., Mrotzek, N., Lemke, U., Hinrichs, J., & Reinsch, K. 2015, ArXiv e-prints, 1511.03014
- Roca Cortés, T. & Pallé, P. L. 2014, *MNRAS*, 443, 1837
- Wallace, L., Huang, Y. R., & Livingston, W. 1988, *ApJ*, 327, 399